Towards realistic characterisation of chemical reactors: An in-depth analysis of catalytic particle beds produced by sieving

Stylianos Kyrimis [a,b], Kathryn E. Rankin [c], Matthew E. Potter [b], Robert Raja [b], Lindsay-Marie Armstrong [a,*]

[a] School of Engineering, University of Southampton, SO17 1BJ, UK
[b] School of Chemistry, University of Southampton, SO17 1BJ, UK
[c] μ-VIS X-ray Imaging Centre, University of Southampton, SO17 1BJ, UK

ABSTRACT

Optimization of large-scale fixed particle bed catalytic reactors requires extensive insight into the multi-scale bed structure, even down to the micrometre scale. Theoretical studies of chemical reactors provide a time- and cost-effective means to supporting the optimisation process. However, they rely on simplified assumptions for the particles, e.g. homogeneous perfect spheres. In practise, the preparation of catalytic particles cannot attain this level of uniformity. Typical preparation techniques, such as sieving, are conducted with the aim of obtaining particle size distributions within a pre-defined range, governed by the sizes of the sieves. However, such methods offer limited control in the actual particle sizes and shapes. This paper evaluates the impact of sieving on the resulting particles and overall structural morphology of catalytic beds. The bed structure is quantified using micro-focus computed tomography (μ-CT), enabling the non-destructive examination and analysis of over 150 thousand particles, in terms of particle size, shape, uniformity, and interparticle porosity. Furthermore, the chemical performance of the resulting beds is compared. The detailed characterisation achieved paves the way for the evolution of more rigorous computational models coupling intricate, localised hydrodynamics with realistic chemical processes. Validation of such models at the lab-scale will accelerate the development of more accurate large-scale models.

© 2022 The Society of Powder Technology Japan. Published by Elsevier B.V. and The Society of Powder Technology Japan. This is an open access article under the CC BY license (http://creativecommons.org/licenses/by/4.0/).

1. Introduction

The design, understanding and optimisation of chemical reactors is vital for improving product yields, bringing significant economic and environmental benefits. While there are many chemical reactor types available, such as batch [1,2], continuous-flow stirred tank [1,3] fluidised or fixed bed [4], and biochemical [1,3], the fixed bed type is primarily used for large-scale heterogeneous gas-phase reactions [5], such as the formation of sulfuric acid, ammonia, and methanol [4]. Their wide utilisation requires a deep understanding and characterisation of their structure, especially given the broad length scales experienced by the physical and chemical processes [5], ranging from the full bed (metre) down to the catalytic active site (nanometre). Fixed beds are typically formed by an array of static and randomly distributed particles [4], that are dropped or poured inside the reactor tube, resulting in a random and potentially unique particle arrangement.

The final structure of the bed is influenced by several key parameters, such as the size and shape of the particles, the N factor, i.e. the dimensionless ratio of reactor tube diameter and particle diameter, and the interparticle bulk, axial, and radial porosities, i.e. the distribution of the interparticle pores within the bed [5,6]. The bed's morphology directly affects all aspects of its hydrodynamic profile, including flow velocity and pressure drop [7–12], heat transfer and temperature profile [9,13], inter- and intraparticle transfer and diffusion [10,14–16], and ultimately chemical performance [14–18]. The reactor's behaviour is an interwoven interaction between all these aspects and, to accurately account for them, it is vital to bridge work on simulated beds and physical packed bed systems, allowing one to fully understand and control the reactor performance.

Several approaches to explore the bed morphology have been developed, most of which are based on beds of spherical particles. Earlier approaches to describe such systems applied semi-empirical correlations, aimed at describing the bed's porosity (either bulk or variation along the radial direction) [19–21] or permeability [22] by utilising perfect spheres. As computational power

---

grew, methods were developed to generate realistic 3D packed beds, most notably the discrete element method (DEM) [6,23,24]. DEM is a numerical model that arranges particles of arbitrary shapes, usually spherical, in a packing structure, by considering the mechanical properties of, and forces applied to, the particles [5,23]. This became one of the predominant methods to study fixed bed chemical reactors, as, unlike semi-empirical correlations, DEM can predict complex local particle arrangements and inhomogeneities in local porosity variations, across various N-factor beds [23]. A limitation of DEM models is the demand for significant computational resources [5,25,26], thus rendering them unsuitable for the evaluation of large-scale reactors. For those scenarios, the porous media modelling approach has been applied, whereby the bed is treated as a single porous continuum with effective volumetric correlations [27]. Unfortunately, the accuracy of this approach is greatly dependant on the suitability and accuracy of the effective properties used to describe the porous continuum [16,23,27,28]. Thus, advancing the development of effective porosity correlations is critical.

Depicting fixed beds solely as structures formed by spherical particles is not often representative of a realistic bed morphology. As such, alternative techniques to observe the structure of real beds have also been used, such as the Scanning Electron Microscopy (SEM) [29] and the Magnetic Resonance Imaging (MRI) [30–32]. These methods have yielded key insights that cannot be observed or produced with monodispersed and homogeneous spherical beds. Boccardo *et al.* used SEM to generate a realistic geometry of real sand samples, and to compare it with a DEM bed which neglects grain polydispersity and irregularity [29]. This study showed that additional parameters should be included in the theoretical correlation, in order to accurately reproduce the experimental data [29]. Mantle *et al.* used 3D MRI and MRI velocimetry to probe the structure of and the flow field through a packed bed of alumina catalytic particles. This was compared with flow simulations performed with the Lattice-Boltzmann method, with the bed structure being incorporated directly from the MRI images. The results showed that flow through the pores is highly heterogeneous, with 40% of fluid flowing through only 10% of the pores [32], something current methods cannot readily account for.

While these techniques are greatly beneficial in offering a unique insight into realistic packed beds, their applications are limited. SEM is limited to only a 2D view of the sample, while MRI detects the heterogeneities of the fluid physical parameters, such as density, filling the interparticle pore space [30,32]. Thus, information regarding the actual catalytic particles is not available. Alternatively, X-ray micro-Computed Tomography (CT) has also been used as a non-destructive method to produce a 3D representation of both regular (spherical) and irregular particles within packed beds. Yang *et al.* [33] used CT to visualise and analyse beds of Copper sulfide particles of various sizes, packed in cylindrical glass columns. They identified that as the size of the ore particles increases, the volumetric porosity, mean pore diameter and the degree of pore connectivity all increased. Using CT, Fernando *et al.* [34] compared the interparticle pore structure and pore network of a packed bed of 16–20 mm irregularly shaped rock particles against a bed of 8 mm spherical glass beads. In addition to observing a 6-fold increase in the number of pores, they found that pores in the spherical bed were much smaller (3.24 mm) compared to those of the irregular bed (5.63 mm), due to the tighter and more efficient packing of the spherical particles. Piovesan *et al.* [35] produced 3D printed polymethylmethacrylate cylinders and used CT to reconstruct the 3D volume, to visualise the interparticle pore network, and to evaluate its permeability. The authors suggested that approximating the interparticle network solely through the default method, i.e. equivalent spheres for the pores and cylinders for the throats, is an oversimplification. Instead, they

suggested the introduction of the pores' sphericity as a factor, method which increased the accuracy of the permeability's prediction. Suzuki *et al.* [36] scanned packed beds comprised of 5 differently sized glass beads with N-factors ranging from 4.6 to 21.5, to investigate the radial porosity distribution and the impact of the wall. The local radial porosity fluctuated significantly near the wall and dampened towards the bed centre, while the period of the fluctuation was dependent on the beads' diameter. For all beds except those with the smallest beads, the amplitude of the oscillations increased near the bed centre, which was attributed to the impact of the opposing side wall on the packing structure. Using these scans, the authors presented a radial porosity empirical correlation, based on an amplitude and a damping factor, which correlated well with the experimental data.

Non-homogeneous and irregular beds increase the complexity of the characterisation, as, unlike perfect spheres, individual particles must be examined. In many fields, such as geology and civil engineering, the actual particle sizes and shapes in naturally formed aggregates are crucial [37,38]. For example, the quality of concrete mix depends on the grading, size, and shape of its aggregates [37]. Similarly, the mechanical behaviour of granular soils is greatly influenced by the particle shapes; thus, accurate characterisation of particle morphology is key to predicting the engineering performance of sand [38]. As a result, several metrics have been proposed, with much debate on which parameters are important and how to best utilise them. Barrett suggests a particle's shape be quantified by three independent properties, its form (overall shape), roundness, and surface texture [39]. In a more recent study, Blott *et al.* consider just two major parameters, namely the particle's shape and surface texture. Here, the particle shape includes four further aspects, particle form, roundness, irregularity, and sphericity, while the surface texture refers to surface features which are small-scale relative to the size of the object [40]. For the quantification of the form, the particle's length (L), breadth (I) and width (S) dimensions are key [40]; however, their utilisation is not always common in the literature [38,41,42]. The form classification proposed by Blott *et al.* uses the combined I/L and S/I ratios of each particle, since, if these ratios are considered individually, they can lead to incorrect assumptions for the particle form [40].

This paper investigates the structure and behaviour of realistic catalysts beds to probe the internal morphology of the catalyst bed whilst providing a means for present and future computational validation. A common multi-step process to control the particle size, especially for packed bed applications, involved initially compressing the catalyst powder into a pellet, crushing and grinding the pellet into particles, and then sieving these particles between predetermined sizes [43–45]. To the best of our knowledge, the impact of the sieving process on the bed structure has not yet been investigated in the literature. Here, the impact of a single and a quintuple sieving process on the particle size distribution is assessed using CT method by analysing six catalytic beds. These are formed by SAPO-34 particles collected with different sieve ranges equal to 100–300 μm, 300–500 μm, and 500–700 μm. Several key metrics are used to quantify the beds, namely the particle size, particle shape, and the beds' interparticle porosity (bulk, radial and axial profiles). Comparisons of these metrics against those for published spherical beds will be made when such are available. This information is then combined to show the influence of sieving processes and particle size on the beds' catalytic performance.

2. Materials and methods used

The six considered catalytic beds are formed from the well-known methanol-to-olefin catalyst, SAPO-34 [46,47], which was

synthesized and characterised according to our previous work [48]. The sieving and packing processes are described herein.

2.1. Particle sieving

The powdered SAPO-34 catalyst was initially pelletised into cylindrical discs, 7 mm in diameter, using a hand press. The pellets were then crushed, grounded, and passed through a tower of differently sized sieves, stacked in a decreasing opening size order, 710 on top, then 500, 300, and finally 106 μm on the bottom (Cole-Palmer, 3″ diameter U.S.A. standard test sieves, No. 25, 35, 50, and 140, respectively). Gentle agitation of the tower encouraged movement of particles through the sieves. The catalyst between two consecutive sieve stacks was then collected, giving three distinct particle sizes, labelled according to the intended particle size range, i.e. 100–300, 300–500, and 500–700 μm. This represents the single-sieve pass case, henceforth referred to as "1S". Another case was also considered, referred to as "5S". Here, the collected particles from each size range, e.g. 300–500 μm, were repeatedly passed through a smaller tower of sieves, e.g. the 500 μm stacked on top of the 300 μm sieve. For these repeated passes, any particles remaining on the upper (i.e. 500 μm) or that passed through the lower sieve (i.e. 300 μm) were discarded, as they were deemed too large or too small, respectively, while the particles in the intended size range were collected and weighed. In between passes, the sieves were dry brushed clean, to remove any dust or remaining particles. This process was repeated until the remaining particles had undergone 5 passes of the sieve stack, each time discarding the undesired particles and dry brushing the sieves. Figure A1 in the ESI shows the percentage of the total particle mass remaining after each sieve pass. The particle mass reaches a plateau after 4 sieve passes, thus, by the 5th pass, larger or smaller particles should have been filtered out.

2.2. Packed bed loading

The reactor tube is identical to that used in previous work [48], a tubular glass reactor with a 4 mm inner diameter and a 6 mm outer diameter (Figure A2). The catalytic particles, 0.30 g in mass, were poured into the top of the reactor, forming a randomly distributed packed bed. During loading, the glass tube was gently agitated to form a more tightly packed bed. Above and below the fixed bed, 1 mm diameter spherical glass beads were placed to fill the reactor. Other than those described, no additional efforts were made to form a more tightly packed bed.

2.3. Computed tomography (CT) scan

The produced beds were analysed with the micro-focus computed tomography μ-CT method at the μ-VIS X-ray Imaging Centre (University of Southampton). X-ray tomography is a non-destructive method of reconstructing the volumetric internal structure of an object from a series of 2D projections, where pixel intensity relates to x-ray attenuation, governed by density [49]. In total, 1601 radiographs were taken as the bed was rotated by 360° around a single axis. The projection data were then reconstructed to produce a volume with a spatial resolution of 6 μm/voxel. Additional information about the equipment used are provided in the ESI. An example of the produced CT images can be seen in Fig. A3a.

2.4. Analysis methodology of the catalytic particles

The Fiji ImageJ [50] and Avizo® (ThermoFisher Scientific) software were used to analyse the CT images. ImageJ was used to concatenate the produced CT volumes, remove noise, distinguish the particles from the background space (interparticle space of the bed), and finally produce a binary image, where particles appear white and interparticle space appears black. ImageJ was then used to evaluate the radial and the axial porosity of the different beds, in a process similar to that described by Mueller [19], Theuerkauf [23] and Suzuki *et al.* [36]. The binary CT images were initially fragmentized into 0.05 mm thick concentric rings, creating a radial area along the height of the bed (e.g. radial area in-between the radial distance of 2.0 mm and 1.95 mm from the bed centre). From this, the "Analyze Particles" function from ImageJ was used [51] to measure the particle area within each radial circle, and compare it to the total area. By integrating the measured radial area over the entire bed, we then estimate the total radial area covered by the particles. In a similar fashion, the bulk porosity (1 - the total solid area), as well as porosity deviations along the axial direction, can be calculated by evaluating the total solid area in each of the produced images and integrating it over the entire bed.

Avizo® v.9.3 was then used for 3D data visualisation and analysis, where the binary 2D slices are combined, and the different particles segmented from their neighbours, to form 3D particles. Once generated, the 3D volumes can be measured and their surface volume can be generated and/or meshed [52]. Several available dimension metrics are provided from Avizo. Here, the particle's length (L), width (S), and breadth (I) (i.e. the longest, shortest, and intermediate diameters of each particle, respectively), equivalent diameter (Eq. Diam.) and sphericity are derived. Further information on these metrics can be found in the ESI (Section 3), while an example of a processed image can be seen in Fig. A3b.

The equivalent diameter metric will be used to quantify the arithmetic and volumetric particle averages for each sieve range. The particle shape will be determined from two of the metrics considered by Blott *et al.* [40], namely the particle form and sphericity (see at ESI, section 3.3, for definition). Other metrics have also been used in the literature, such as the roundness and the irregularity, [40], or the convexity ratio [37,38] However, evaluating these metrics with the available methodology would not be possible without further assumptions and simplifications. Finally, the measured interparticle bed porosity, i.e. bulk and radial or axial profiles, is compared with the semi-empirical correlations of de Klerk [20] and of Patil [53], produced from homogeneous spherical beds (section 1, ESI).

2.5. Chemical performance

Following our previous work [48,54,55], the chemical performance of the different catalytic beds was evaluated with ethanol dehydration as the baseline reaction, as per section 2.2 of the ESI. Here, a temperature range of 185–220 °C is considered, with intervals of 5 °C, and a Weight Hourly Space Velocity (WHSV) of 2 h^{-1}. The results presented are an average of duplicate runs.

3. Results and discussion

Out of the 6 total beds studied, detailed description and data is primarily presented here for the 1S and 5S 300–500 μm beds. The respective data for the 100–300 μm and 500–700 μm beds, resulting from both the 1S and 5S processes, are presented in the ESI. However, all 6 beds are discussed and compared.

3.1. Controlling the particle size

Fig. 1 shows the reconstructed 3D volumes of the 1S and 5S 300–500 μm cases, which represent a 10% section of the entire bed volume located at an approximate depth in-between 1.6 and 1.9 cm. 2D side- and top-view images for all beds are presented in the ESI (Figures A4-A6). Throughout, the colour scheme used

a) 1S – 300-500 µm
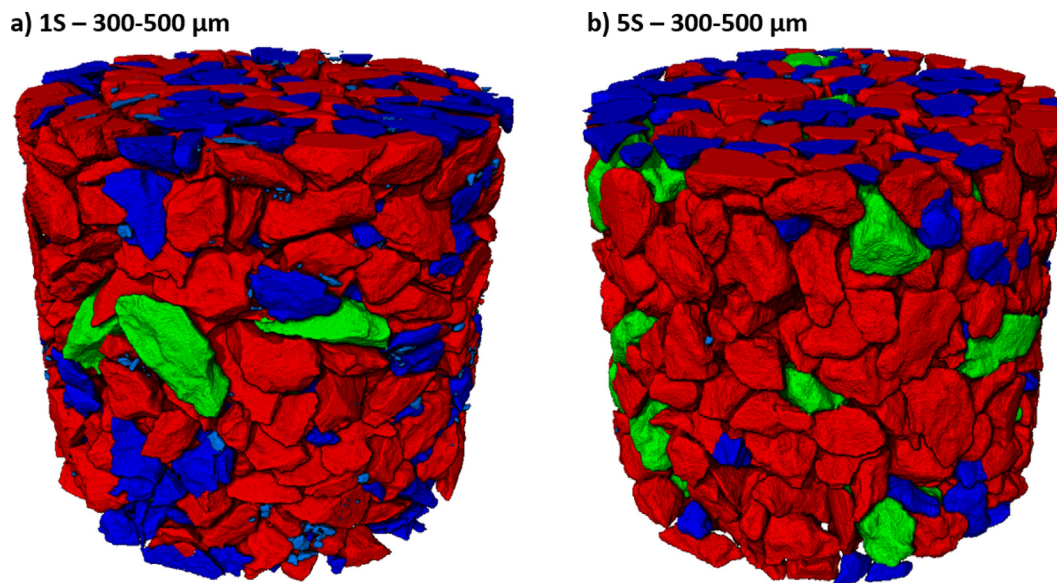
b) 5S – 300-500 µm

Fig. 1. Reconstructed 3D volume from the analysed CT pictures of a) the 1S and b) the 5S 300–500 µm cases. The reconstructed volume accounts for 10% of the total bed volume, located in the middle section (at a depth in-between 1.6 and 1.9 cm). The particles are coloured according to their equivalent diameter, with cyan < 100 µm, blue 100–300 µm, red 300–500 µm, and green 500–700 µm. (For interpretation of the references to colour in this figure legend, the reader is referred to the web version of this article.)

for the different particles indicates their equivalent diameter, following the connotation: cyan: < 100 µm, blue: 100–300 µm, red: 300–500 µm, green 500–700 µm, and yellow: >700 µm. It can be observed that the beds consist of a range of irregular particle shapes and sizes, deposited in random orientations. However, Fig. 1 cannot reveal much quantitatively for direct comparisons between the two beds, and further in-depth analysis of the individual particles is required.

Fig. 2a presents the impact of the sieving process (1S and 5S) on the particle population distribution by plotting each particle's length (L - longest measured particle diameter) and width (W - smallest measured particle diameter) dimensions. By definition, no particles exist above the L = W line. Fig. 2a is subdivided into several zones (discussed in detail in the ESI, Figure A7), and the population of each zone is shown in Fig. 2b. Fig. 2c and Fig. 2d present the particle size distribution and their respective volume coverage, respectively, based on their equivalent diameters. The respective data for the 100–300 µm and 500–700 µm beds, as well as the volumetric average values for the four considered metrics used to quantify the particle dimensions, are presented in the ESI (Figures A8-A9 and Table A1).

The multiple sieving of the 5S process had a significant impact on the particle size distributions (Fig. 2a). The 1S particles have a wider range of lengths and widths whereas the 5S particles appear to have a narrower size distribution, suggesting that the multiple sieving had the intended effect. This is also shown in the populations of the different zones (Fig. 2a and Fig. 2b). Zone A represents the ideal size zone for particles to occupy, based on the sieve ranges used, where both length and width are between 300 and 500 µm. The population of this zone increased from 0.7% (1S) to 2.2% (5S), suggesting the 5S process does help filter out undesired particles. The very low population of this zone is due to the mainly irregular shapes of our particles, where the length and width dimensions are not necessarily proportional. This was already confirmed by Fig. 1, as many of the particles appear to have a "rod-like" shape, thus occupying the remaining zones instead.

Zone B represents the region where only one of the two dimensions falls into the 300–500 µm range. Here, we see a significant population increase from 12% (1S) to 52% (5S). Therefore, most of

the particles in the 5S system fall into either Zone A or B, showcasing the noticeably narrower particle distribution due to more thorough sieving. Zone C represents particles whose both length and width are below the lowest sieve range (300 µm). In all cases, for the vast majority of these particles, their dimension metrics are less than 100 µm; these particles will be henceforth referred to as dust particles. In an ideal system, such dust particles should not appear within the reactor bed, as they should have been filtered out through the lowest sieve (300 µm in this case). Despite this, they have a significant population in 1S (61%), which is greatly reduced with 5S (19%), showing a dramatic reduction but not a complete removal on enhanced sieving. We suggest that these smaller particles come from either particles cracking or fracturing on being transferred within the reactor, or are residing as a "dust-like" coating on top of larger particles. However, the repeated agitation of the 5S process would shake off most of dust prior to the catalyst being loaded into the reactor.

Zone D represents particles whose length is larger than the upper sieve range (>500 µm) while the width is smaller than the lower sieve range (<300 µm). The appearance of particles here seems to depend on the particles' orientation during sieving, specifically, being able to pass through the upper sieve (500 µm), then rotating and changing their orientation before landing flat on the lower sieve (300 µm) and getting trapped there. Surprisingly here, the population increases from 13% (1S) to 18% (5S), however, in terms of absolute population rather than percentage, the 1S has 2.6 k particles in this zone, which is reduced to 1.5 k in the 5S. This emphasises the need to consider both absolute and percentage populations. The final zone, Zone E, is occupied by particles whose both length and width dimensions are larger than the upper sieve size (>500 µm), which is theoretically not possible. However, in both cases, this represents <1.5% of the total population, suggesting it is not making a significant contribution to either of the beds. Overall, the data in Fig. 2a and Fig. 2b confirms that the extra sieving of the 5S process does drastically lower the size distribution of the particles in the bed, compared to the 1S process. Table A1 reinforces this, as here, the 5S bed has a narrower average range between the particle length and width, of 711 ± 20 and 374 ± 10 µm, respectively, whereas the 1S bed has a wider
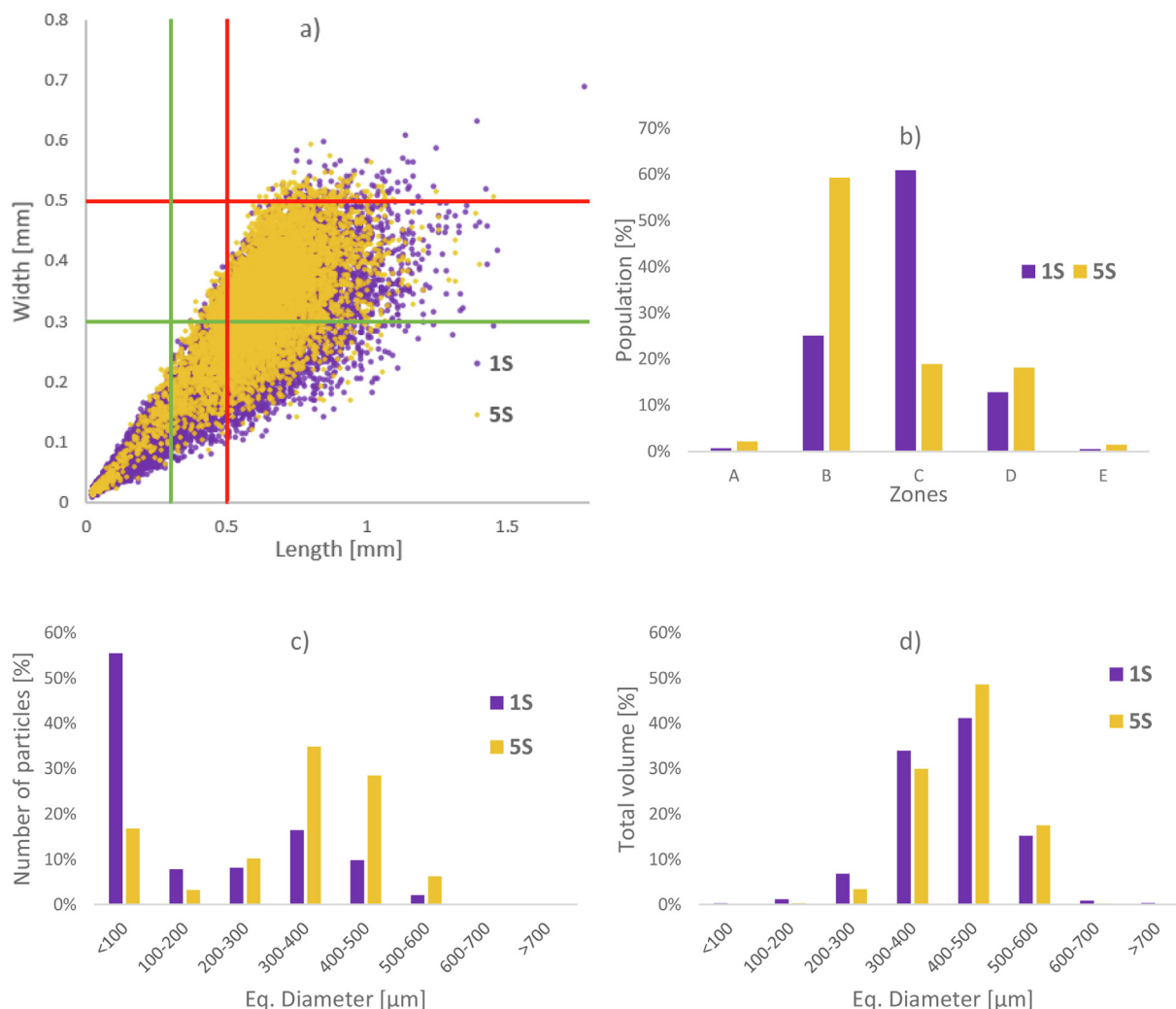
Fig. 2. a) Impact of the 1S and 5S sieving processes on the particles length and width distribution on the 300–500 μm bed and b) population of particles per zone. The particle size distribution and volume coverage are shown in c) and d), respectively, with the eq. diameter as the metric. Population size is ≈20.4 k and ≈8.4 k for the 1S and 5S beds, respectively.

range with the average length and width being 747 ± 18 and 352 ± 8 μm, respectively. Both results are indicative of the increased uniformity and narrower size distribution achieved in the 5S bed.

Fig. 2c and Fig. 2d shows the distribution of particle sizes, measured through the equivalent diameter (section 3.1, ESI), by considering the percentage population and volume coverage, respectively, from the 1S and 5S processes. While the equivalent diameter is measured by over-simplifying each particle as a sphere, it is a useful metric when an average particle size should be considered. Here, it is also evident that the 5S achieves a narrower particle size distribution volume-wise when compared to 1S (Fig. 2d), while the majority of the volume occupied by the intended 300–500 μm size is increased from 75% (1S) to 79% (5S). We also notice that despite dust particles having a significant population in both beds as per Fig. 2c, with 56% in 1S and 17% in 5S, their volume coverage, Fig. 2d, is almost negligible (<0.3%).

Looking at the 1S and 5S 100–300 μm beds (Figure A8), similar trends can be seen. Comparing the length and width distribution of particles, the 5S bed again occupies a narrower size range. The increased uniformity in the particle sizes is also shown by the smaller range in-between the average length and width of the particles, as per Table A1, which is 413 ± 2 and 189 ± 1 μm, respectively, for the 1S bed and 396 ± 2 and 210 ± 1 μm, respectively,

for the 5S bed. Considering the zone populations for the 1S and 5S cases, the sum of zones A and B are 54% and 95%, respectively, while for zone C is 45% and just 4%, respectively. For both 1S and 5S beds, populations of zone D and E were below 1.5%. Similarly, the equivalent diameter distribution is narrower for 5S, again demonstrating the uniformity of the 5S bed compared to the 1S bed.

In the 1S and 5S 500–700 μm beds (Figure A9), in terms of percentage population, 5S has more particles in zones A and B, equal to 52%, compared to 1S, with 12%, whereas the particles in zone C are also greatly reduced from 79% (1S) to 16% (5S). The particles of zone D are seemingly more in 5S, with 30%, compared to 1S with 9%, but in terms of absolute numbers, the two are very similar (840 in 1S, 750 in 5S). While the 5S bed achieves a narrower distribution, there are less distinctions between the 1S and 5S methods here compared to what was seen in the other two sieve sizes. This is evident by inspecting the average particle length and width of the particles, Table A1, which is equal to 1016 ± 53 and 523 ± 27 μm, respectively, in the 1S, and 1028 ± 83 and 549 ± 44 μm, respectively, in the 5S bed; the size range in 5S is smaller, suggesting more uniform particles. However, these differences are within experimental error. Furthermore, while the equivalent diameter distribution is narrower in the 5S bed (Figure A9), particles of almost all sizes exist within both. The existence of a
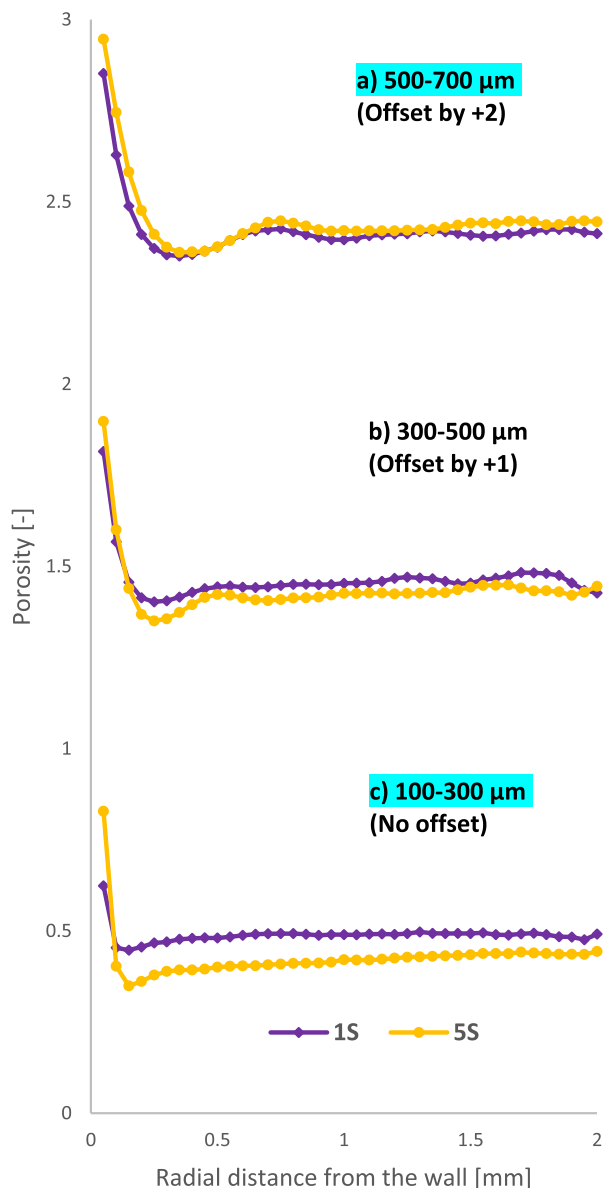
Fig. 3. Radial porosity profiles of the 1S and 5S a) 500–700, b) 300–500, and c) 100–300 μm cases. The 500–700 and 300–500 μm cases have been offset by + 2 and + 1, respectively.

wide particle size distribution here suggests that these are not the result of inefficient filtering, but rather of larger particles fracturing into smaller pieces. This further supports the argument of dust being caused by particle cracking. If this result was instead caused from poor sieving, similar wide distributions would also be observed in the other beds.

With the above analysis in mind, it can be concluded that the additional sieve passes of the 5S method allow for more accurate control of the particle size loaded within the reactor and help to reach better particle homogeneity. This is a highly desirable effect, as accurate control of the particle size enables more precise studies and theoretical estimations, where the aspect of randomness is reduced to a few parameters (such as deviation from complete particle homogeneity and shape factor). Most DEM studies of chemical reactors consider homogeneous particles, in the shape of spheres. While additional sieve passes can help with the aspect of homogeneity, they have no control in the particle shape, thus the particles could deviate significantly from perfect spheres. This aspect of the produced particles is discussed in the following section.

3.2. Quantifying the particle shape

Blott's form classification is based on the particles' I/L and S/I dimension ratios, with each of them varying between 0 and 1. A value of 1 in both ratios indicates a perfect shape, e.g. a sphere or a cube, while smaller ratios indicate elongated elliptical or cuboid/trapezoid forms. If both the particle's I/L and S/I ratios are above 0.6, then this will classify it as either a sub-equant or an equant block. Table 1 presents the particle population with both S/I and I/L Blott ratios above 0.6 (Figure A10 in ESI). The dust particles (<100 μm) were excluded from this analysis. Due to their small size, the I/L and S/I ratios were very close together, leading to an un-realistic shift of the particle population towards more equant forms. However, while they affected the population coverage of each classification, the overall trends of which Blott classifications are more heavily populated remained. Therefore, in addition to their volumetric coverage being so small, their contribution was considered negligible.

The 5S beds all have a similar proportion of particles with I/L and S/I ratios above 0.6, between 70 and 74%, regardless of the sieving range. On the contrary, the 1S beds have less particles in this range, with the 100–300 and 300–500 μm beds having 50 and 51%, respectively, and the 500–700 μm bed having 63%. In all cases, the "Flat Block" and "Elongate Block" regions also contain a reasonable number of particles, further supporting the finding of the previous analysis, as much of these particles have disproportionate shapes and can occupy either zones B or D. Despite the majority of the particles having a sub-equant or equant form, they are not spherical but rather blocks, as shown in Fig. 1.

To probe this further, the average volumetric sphericity of the particles was evaluated and presented in Table 1. Sphericity has a maximum possible value of 1, representing a perfect sphere. We note that small particles, only few voxels in size, were found to have a theoretically impossible sphericity value>1 (Figure A11-A17). This is because of the different approach Avizo uses to approximate the area and the volume of a 3D particle [52], both of which are necessary to measure the particle's sphericity (section 3.3.2, ESI, for more details). Therefore, such particles were excluded from this calculation. In all cases, the average volumetric sphericity was found to be between 0.68 and 0.73, while, as seen on Figures A11, A13, and A15, as the equivalent diameter of the particles increases, they seem to reach a sphericity plateau between 0.6 and 0.8. The results of both analyses clearly demonstrate that the particles are indeed irregular and considering them simply as perfect spheres is an oversimplification of their shape.

The presented analyses also showcase the efficiency of the 5S process in filtering out irregular particles. However, for both metrics, the particles seem to reach an upper plateau, suggesting that the sieving itself is not the driving factor of the particle shape. Apart from sieving, generating the particles involves two additional steps, compression and grinding. As the standard 7 mm pellet produced from compression is continuously grounded down to the μm scale, it is unlikely that this step significantly contributes to

Table 1
Particle population with Blott ratios > 0.6 and volumetric sphericity and for all 6 considered beds.

Particle size (μm)	Bed case	Populations with Blott ratios > 0.6	Volumetric sphericity
100–300	1S	50.2%	0.68 ± 0.01
	5S	73.3%	0.73 ± 0.01
300–500	1S	51.2%	0.70 ± 0.01
	5S	70.1%	0.73 ± 0.02
500–700	1S	62.9%	0.71 ± 0.03
	5S	71.9%	0.73 ± 0.05

the final particle shape. Conclusively, the primary driving factor of the particle shape is the grinding process, which offers limited control in its modification.

3.3. Porosity profile along the catalytic bed

With the produced CT scan images, it is also possible to evaluate the volumetric porosity of the beds, in both the radial and the axial direction. The radial porosity profiles for the 1S and 5S 100–300, 300–500, and 500–700 μm beds are presented in Fig. 3. Table A2 presents the bulk porosity of all 1S and 5S beds, along with the theoretical bulk porosity estimated from the semi-empirical correlations of Achenbach [56] and Dixon [57]. The particle diameter, necessary to calculate the correlations (section 1, ESI), was considered equal to the respective equivalent diameter of the particles in the 5S beds.

The radial porosity profiles seen in Fig. 3 follow the general trends described in the literature [5,19,20]. Namely that: a) the minimum porosity value is observed at roughly half a particle diameter from the wall, b) away from the wall, radial porosity presents dampening oscillations, c) the oscillations amplitude is proportionally related to the particle size, with smaller particles reaching a smoother radial profile earlier, and d) the reactor tube wall has a greater influence on larger particles. Comparing the radial porosities of the different beds, we can see that the oscillations become more prominent for the larger particle beds. The 100–300 μm beds show no significant oscillations; after reaching the global minima, the radial porosity smoothly increases and converges, with the 5S bed reaching an overall lower porosity magnitude. In contrast, the 500–700 μm has several clearly defined oscillations beyond the global minima. The 300–500 μm beds exist in-between the other two beds, with a well-defined initial oscillation down to the global porosity minimum, which converges soon after. All these effects are indicative of the impact of the wall on the bed structure, and its relation to the particle size. Regardless of whether the particles are perfect spheres, as seen in the literature [19,20], or have inhomogeneous sizes and shapes, as seen here, the wall induces similar constraints in the resulting bed morphology.

Both the 5S 100–300 μm and 300–500 μm beds reached a lower radial porosity profile and a lower bulk porosity (Table A2) than the 1S beds, suggesting more efficient packing is achieved in the 5S bed. This further supports the notion that the 5S process filters out irregular particles, leading to those remaining having higher Blott ratios and sphericity values. Regular particles are more efficiently packed than irregular particles, as seen by Fernando *et al.* [34] as well, where a bed of perfect spherical beads was more efficiently packed and achieved a lower porosity than a bed formed from irregular porous rock particles. This can further be emphasized by comparing the bulk porosity of the 1S and 5S beds with the theoretical bulk porosity of a bed of spheres, estimated from the correlations of Achenbach [56] and Dixon [57] (Table A2). The bulk porosity of the 5S 100–300 μm and 300–500 μm are both closer to the theoretical correlations, compared to the respective 1S beds, again showing the higher particle uniformity and regularity achieved by the 5S process, bringing this bed closer to an ideal theoretical model. This seems to not be the case for the 500–700 μm bed, however, as the 1S bed achieves a lower bulk porosity than the 5S bed. As seen in Figure A9d, both 1S and 5S beds consist of a wider range of particle sizes, attributed to particle fracturing, thus not achieving the same size homogeneity as the other two beds. As a result, the packing structure of the 500–700 μm bed will inherently be more random. Furthermore, it is worth mentioning that a small volume of the 1S 500–700 μm bed was removed during analysis; this is due to the existence of a 1-mm glass bead within the bed structure. Despite porosity being evaluated as a volume fraction, the existence of this oversized glass bead will

significantly modify the local porosity variation, pushing local particles into a tighter packing.

Despite our radial porosity profiles showing similar trends to the literature, they also have stark differences when directly compared to the theoretical radial profiles of de Klerk [20] and of Patil *et al.* [53], both of which were defined for spherical particles (Fig. 4 and Figure A17). To calculate these correlations, the average equivalent diameter and bulk porosity of the 5S beds were used, as they achieved a higher particle size homogeneity. While Patil's correlation predicts the radial distance and magnitude of the first global minimum better than de Klerk's correlation, both predict oscillations with significantly larger amplitudes and periods compared to those of the actual beds. The radial profiles of the actual beds appear smoother than the correlations, as the local porosity variations are averaged out; some oscillations however do appear closer to the bed centre. To better understand the vast differences in the oscillating profiles between experiments and correlations, the local profile inhomogeneities for the 1S and 5S 300–500 μm beds were investigated. These focused on both the axial variation of the bulk porosity (Figure A19) and the axial variation of the radial porosity profiles (Figures A20 and A21), with the latter being investigated at four axial slices of 0.2 axial length thickness. Along the axial direction, the beds present oscillations that vary significantly, with magnitudes of up to 0.07, in a seemingly random fashion. Also, in their radial profiles, oscillations are present along the entire radial length and do not converge in the near-central region. All these radial and axial features are cancelled out during the averaging process, resulting in a volumetric radial profile that seems constant. An argument against semi-empirical porosity correlations is that they are unable to capture local inhomogeneities compared to DEM models [23]. We would argue that this is because the axial aspect of particle beds is usually omitted, instead focusing only on the definition of a radial correlation that is volumetrically constant. While our beds seem featureless along the axial direction, this might not be the case for spherical beds. Investigating such beds closer to consider both the bulk porosity and the radial profile variation along the axial direction could reveal regularly repeating patterns, leading to the generation of novel and more complex correlations.

This discussion emphasizes that the available semi-empirical correlations, based on perfect beds of spheres, are an oversimplification, and brings forth the question of what parameters would be crucial for future correlations to include. It is not possible to answer this with our data, as this requires a systematic investiga-
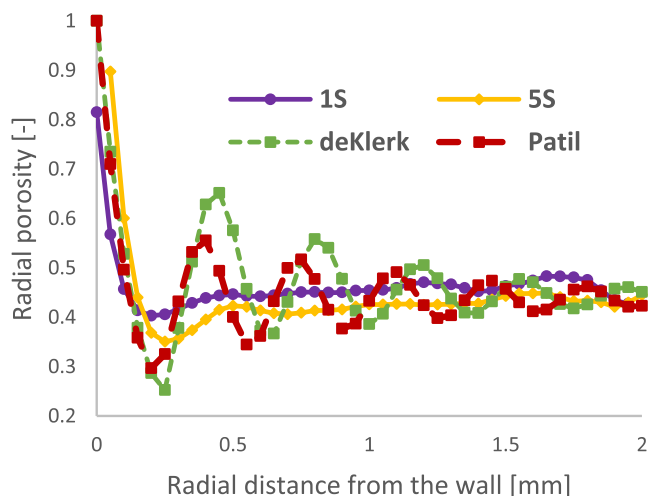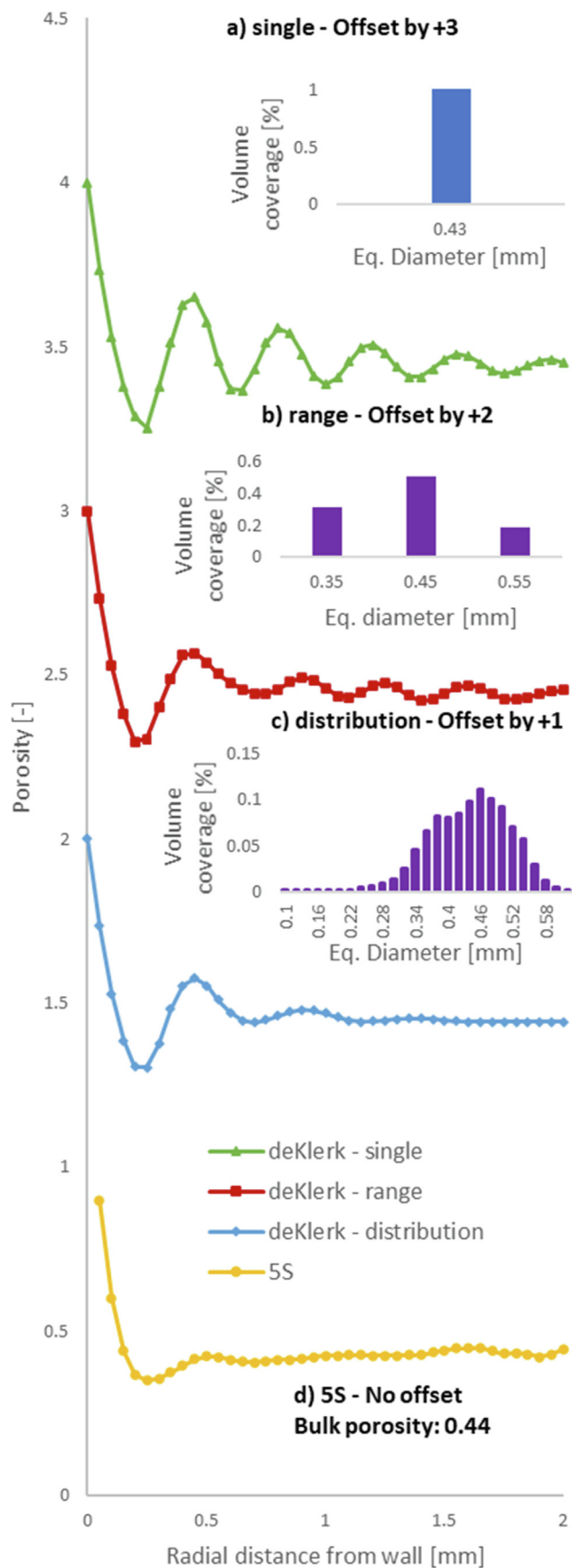

Fig. 4. Comparison of measured radial porosity profiles of the 1S and 5S 300–500 μm beds with the correlations of de Klerk [20] and of Patil [53].

Fig. 5. Profile of the semi-empirical correlation of de Klerk [20], when a) a single, b) a range of three, and c) a distribution of equivalent diameters, estimated from the 5S 300–500 μm bed, are considered. In the top right-hand side of each figure, the equivalent diameter range used for each correlation is presented. In addition, the radial profiles of the 5S 300–500 μm cases are presented in d.

tion of key particle parameters, such as size, shape, and orientation. However, the incorporation of a range of particle sizes into the correlation, instead of a single average size, can be further investigated here. This possibility was explored using the correlation of de Klerk [20] by gradually increasing the size range of the considered particles, as Patil's correlation is primarily focused on fluidised beds instead of packed beds [53]. In Fig. 5a, the correlation is estimated by considering only a single value for the equivalent diameter, equal to the volumetrically average equivalent diameter of the 5S 300–500 μm bed, in addition to its bulk porosity. In Fig. 5b, the presented correlation is a combination of three distinct correlations. In each of these, the respective particle size is equal to one of the three predominant equivalent diameters of the 5S 300–500 μm bed, as per Fig. 2d and Figure on top right-hand side of Fig. 5b, normalised by their volumetric coverage. The three produced correlations are then added together. Similarly, in Fig. 5c, the equivalent diameter is considered as a distribution (graph at the top right-hand side of Fig. 5c), and the presented correlation is the sum of each individual size, normalised by the respective volume coverage. As a comparison, the radial porosity profiles of the 1S and 5S beds are also presented. It is evident that the wider the particle size range considered, the closer the correlation gets to the experimental data. The magnitude of the oscillations is gradually reduced, and the profiles flatten towards the bed centre because of the summation of opposing radial profiles. This is similar to the effect taking place in the actual catalytic beds. In addition, the position of the peaks now shifts, except for the global minimum and maximum peaks which remain on a similar radial length. The results seen here confirm that simple modifications to the correlations can positively affect their prediction accuracies for more realistic bed morphologies. Further modifications could focus on introducing the particle shape as a factor.

3.4. Chemical performance

The influence of the different sieving methods on the chemical performance was investigated by considering ethanol dehydration as the baseline reaction. Potter et al. [48] showed that ethanol readily forms a diethyl ether intermediate, which is then slowly converted into ethylene. As the produced ethylene does not react further, its outlet concentration, shown in Fig. 6, serves as a good representation of the activity and the reaction rate of the catalytic beds.

Comparatively to the 1S beds, all 5S beds reach a greater ethylene concentration, showcasing that the impact of the sieving process does not only affect the bed morphology but also its catalytic behaviour. In fact, here, sieving is more influential than the particle size, the latter of which shows very little variation in the chemical activity. Particle size is known to cause diffusion limitations [3], however pore-diffusion might not be rate limiting under the conditions considered in this study. While the difference in their catalytic performance is evident, at this point, there are not enough data to speculate a reason for the observed behaviour. The 5S process significantly affected the particle homogeneity within the bed,
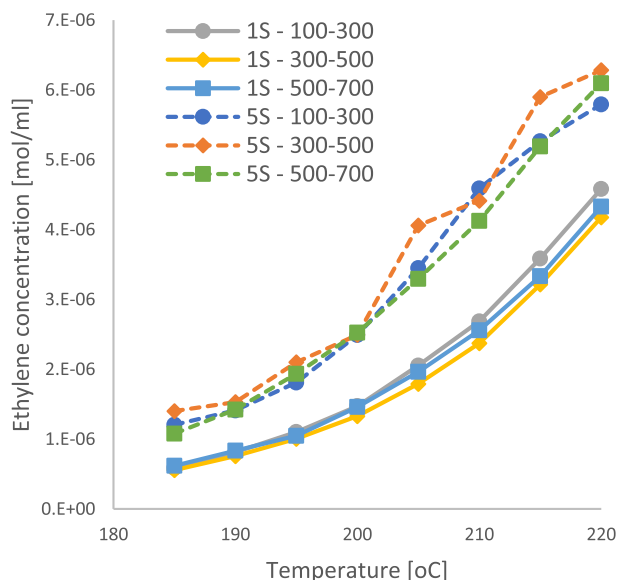
Fig. 6. Ethylene concentration at the outlet of the reactor, for both 1S and 5S beds and for all particle sizes.

however, there are several other factors that could affect the bed's performance, e.g. the existence of dust particles, the particle shapes, and the particle orientations with respect to the incoming flow.

Trying to understand the chemical performance of the beds by simply investigating the species at the outlet of the reactor creates an incomplete picture. Unfortunately, experimental *in-situ* knowledge of other operating parameters, such as local temperature and pressure, are very hard to measure non-invasively. As a result, alternative methods are required. CFD models are a potential option, as they have already demonstrated they are capable of accurate and complex investigations and predictions when applied to chemical reactors [48,58]. The authors are currently conducting dedicated CFD investigations at the single particle scale to describe the behaviour observed here. Instead of a perfect sphere, the particle could be modelled as a block, ideally with some irregularities in its shape, e.g. pointy edges, and placed at various orientations with respect to the incoming flow. With this method, the physicochemical phenomena, e.g. diffusion and reaction, will be coupled with the particle size, shape, and orientation, thus yielding key observations. Furthermore, the reproduced full-bed 3D geometry from Avizo can be meshed and utilised with a CFD model to investigate the various flow fields, as well as their complex interactions, around and within the actual catalytic particles. With this approach, the impact of the inhomogeneous particle sizes, shapes, and orientations on the local and global temperature and pressure, inter- and intraparticle diffusion, and chemical reaction will be accounted for, thus allowing for a unique insight that cannot be reproduced with models based on homogeneous spherical particles. Combining such a study with the analysis presented here will offer a well-rounded picture of all aspects and processes governing the operation of small-scale chemical reactors and enable the development of more accurate large-scale models.

4. Conclusions

Characterising and understanding fixed bed chemical reactors at small scales is crucial for large-scale optimization studies. The bed structure and porosity have been characterised in the literature through the study of beds formed by homogeneous spherical particles. However, here, information about individual catalytic particles and the internal bed structure they form is received through computed tomography scans. By pelletising, grinding, and sieving SAPO-34 catalytic powder, particles of predetermined sizes are produced. The produced particles, before being loaded into the reactor, were sieved either once or five times into three different sieve fractions, forming six distinct bed structures. Multiple sieving passes greatly reduced the amount of dust particles within the bed, while also allowing a more homogeneous distribution of particle sizes. However, the sieving process itself had limited impact on the shape of the particles, which is determined by the grinding process. In addition, while most of the particles had a sub-equant or equant form, their sphericity indicated that approximating them as spheres is an oversimplification.

The interparticle bed porosity for all beds was also measured and their radial profiles were compared with those produced with semi-empirical correlations for beds of spheres. Due to the oversimplification of the particle size and shape into homogeneous spheres, the theoretical radial profiles presented significant deviations from the actual profiles measured here. This led to a preliminary investigation on how these correlations may be modified to account for inhomogeneities within a bed. This distinction emphasizes even more that a complete bed characterisation is a multifaceted project, which includes and involves several different scientific fields. As systems, fixed bed chemical reactors incorporate three distinct aspects, namely the bed structure, the chemical performance, and the various flow fields. It is impossible to consider these aspects in isolation and not consider their interconnected interactions. Thus, to fully understand and characterise them, all these aspects should be investigated in depth.

Declaration of Competing Interest

The authors declare that they have no known competing financial interests or personal relationships that could have appeared to influence the work reported in this paper.

Appendix A. Supplementary data

Supplementary data to this article can be found online at https://doi.org/10.1016/j.apt.2022.103932.

References

[1] S.H. Fogler, Elements of Chemical Reaction Engineering, fifth ed., Pearson, 2016.

[2] K.A. Coker, Chapter Four - Industrial and Laboratory Reactors, in: A.K. Coker, C.A. Kayode (Eds.), Modeling of Chemical Kinetics and Reactor Design, Gulf Professional Publishing, Woburn, 2001, pp. 218–259.

[3] E.B. Nauman, Chemical Reactor Design, Optimization, and Scaleup, second ed., Wiley, 2007 October 2007.

[4] R.W. Missen, C.A. Mims, B.A. Saville, Introduction to Chemical Reaction Engineering and Kinetics, Wiley, 1999.

[5] A.G. Dixon, M. Nijemeisland, E.H. Stitt, Packed Tubular Reactor Modeling and Catalyst Design using Computational Fluid Dynamics, Computational Fluid Dyn. 31 (2006) 307–389.

[6] G.E. Mueller, Numerically packing spheres in cylinders, Powder Technol. 159 (2) (2005) 105–110.

[7] R.E. Hayes, A. Afacan, B. Boulanger, An equation of motion for an incompressible Newtonian fluid in a packed bed. 18(2) (1995) 185-198.

[8] H. Bai, J. Theuerkauf, P.A. Gillis, P.M. Witt, A Coupled DEM and CFD Simulation of Flow Field and Pressure Drop in Fixed Bed Reactor with Randomly Packed Catalyst Particles, Ind. Eng. Chem. Res. 48 (8) (2009) 4060–4074.

[9] A. Guardo, M. Coussirat, M.A. Larrayoz, F. Recasens, E. Egusquiza, Influence of the turbulence model in CFD modeling of wall-to-fluid heat transfer in packed beds, Chem. Eng. Sci. 60 (6) (2005) 1733–1742.

[10] P. Magnico, Hydrodynamic and transport properties of packed beds in small tube-to-sphere diameter ratio: pore scale simulation using an Eulerian and a Lagrangian approach, Chem. Eng. Sci. 58 (22) (2003) 5005–5024.

[11] J. Tobiś, Influence of bed geometry on its frictional resistance under turbulent flow conditions 55(22) (2000) 5359–60.

[12] J. Tobiś, Modeling of the Pressure Drop in the Packing of Complex Geometry, Ind. Eng. Chem. Res. 41 (10) (2002) 2552–2559.

[13] S.J.P. Romkes, F.M. Dautzenberg, C.M. Van Den Bleek, H.P.A. Calis, CFD modelling and experimental validation of particle-to-fluid mass and heat transfer in a packed bed at very low channel to particle diameter ratio. 96(1–3) (2003) 3-13.

[14] T. Maffei, G. Gentile, S. Rebughini, M. Bracconi, F. Manelli, S. Lipp, et al., A multiregion operator-splitting CFD approach for coupling microkinetic modeling with internal porous transport in heterogeneous catalytic reactors, Chem. Eng. J. 283 (2016) 1392–1404.

[15] A.G. Dixon, M.E. Taskin, M. Nijemeisland, E.H. Stitt, CFD Method To Couple Three-Dimensional Transport and Reaction inside Catalyst Particles to the Fixed Bed Flow Field, Ind. Eng. Chem. Res. 49 (19) (2010) 9012–9025.

[16] A.G. Dixon, Local transport and reaction rates in a fixed bed reactor tube: Endothermic steam methane reforming, Chem. Eng. Sci. 168 (2017) 156–177.

[17] X. Zhou, Y. Duan, X. Huai, X. Li, 3D CFD modeling of acetone hydrogenation in fixed bed reactor with spherical particles, Particuology 11 (6) (2013) 715–722.

[18] A. Richter, P.A. Nikrityuk, B. Meyer, Three-dimensional calculation of a chemically reacting porous particle moving in a hot O2/CO2 atmosphere. 83 (2015) 244-258.

[19] G.E. Mueller, Radial void fraction distributions in randomly packed fixed beds of uniformly sized spheres in cylindrical containers, Powder Technol. 72 (3) (1992) 269–275.

[20] A. de Klerk, Voidage variation in packed beds at small column to particle diameter ratio, AIChE J. 49 (8) (2003) 2022–2029.

[21] S. Li, Y. Ding, D. Wen, Y. He, Modelling of the behaviour of gas–solid two-phase mixtures flowing through packed beds, Chem. Eng. Sci. 61 (6) (2006) 1922–1931.

[22] B. Yang, T. Yang, Z. Xu, H. Liu, X. Yang, W. Shi, Impact of Particle-Size Distribution on Flow Properties of a Packed Column, J. Hydrol. Eng. 24 (3) (2019) 04018070.

[23] J. Theuerkauf, P. Witt, D. Schwesig, Analysis of particle porosity distribution in fixed beds using the discrete element method, Powder Technol. 165 (2) (2006) 92–99.

[24] G.E. Mueller, Numerical simulation of packed beds with monosized spheres in cylindrical containers, Powder Technol. 92 (2) (1997) 179–183.

[25] D. Jajcevic, E. Siegmann, C. Radeke, J.G. Khinast, Large-scale CFD–DEM simulations of fluidized granular systems, Chem. Eng. Sci. 98 (2013) 298–310.

[26] G.D. Wehinger, T. Eppinger, M. Kraume, Detailed numerical simulations of catalytic fixed-bed reactors: Heterogeneous dry reforming of methane, Chem. Eng. Sci. 122 (2015) 197–209.

[27] O. Laguerre, S. Ben Amara, G. Alvarez, D. Flick, Transient heat transfer by free convection in a packed bed of spheres: Comparison between two modelling approaches and experimental results, Appl. Therm. Eng. 28 (1) (2008) 14–24.

[28] S.T. Kolaczkowski, R. Chao, S. Awdry, A. Smith, Application of a CFD Code (FLUENT) to Formulate Models of Catalytic Gas Phase Reactions in Porous Catalyst Pellets, Chem. Eng. Res. Des. 85 (11) (2007) 1539–1552.

[29] G. Boccardo, D.L. Marchisio, R. Sethi, Microscale simulation of particle deposition in porous media, J. Colloid Interface Sci. 417 (2014) 227–237.

[30] B. Manz, L.F. Gladden, P.B. Warren, Flow and dispersion in porous media: Lattice-Boltzmann and NMR studies, AIChE J. 45 (9) (1999) 1845–1854.

[31] J. Götz, K. Zick, C. Heinen, T. König, Visualisation of flow processes in packed beds with NMR imaging: determination of the local porosity, velocity vector and local dispersion coefficients, Chem. Eng. Process. 41 (7) (2002) 611–629.

[32] M.D. Mantle, A.J. Sederman, L.F. Gladden, Single- and two-phase flow in fixed-bed reactors: MRI flow visualisation and lattice-Boltzmann simulations, Chem. Eng. Sci. 56 (2) (2001) 523–529.

[33] B.-H. Yang, A.-X. Wu, X.-X. Miao, J.-Z. Liu, 3D characterization and analysis of pore structure of packed ore particle beds based on computed tomography images, Trans. Nonferrous Met. Soc. Chin. 24 (3) (2014) 833–838.

[34] W.A.M. Fernando, I.M.S.K. Ilankoon, A. Rabbani, M. Yellishetty, Inter-particle fluid flow visualisation of larger packed beds pertaining to heap leaching using X-ray computed tomography imaging, Miner. Eng. 151 (2020).

[35] A. Piovesan, C. Achille, R. Ameloot, B. Nicolai, P. Verboven, Pore network model for permeability characterization of three-dimensionally-printed porous materials for passive microfluidics, Phys. Rev. E 99 (3) (2019).

[36] M. Suzuki, T. Shinmura, K. Iimura, M. Hirota, Study of the Wall Effect on Particle Packing Structure Using X-ray Micro Computed Tomography, Adv. Powder Technol. 19 (2) (2008) 183–195.

[37] C.F. Mora, A.K.H. Kwan, Sphericity, shape factor, and convexity measurement of coarse aggregate for concrete using digital image processing, Cem. Concr. Res. 30 (2) (2000) 351–358.

[38] L. Li, M. Iskander, Comparison of 2D and 3D dynamic image analysis for characterization of natural sands, Eng. Geol. 290 (2021).

[39] P.J. Barrett, The shape of rock particles, a critical review, Sedimentology 27 (3) (1980) 291–303.

[40] S.J. Blott, K. Pye, Particle shape: a review and new methods of characterization and classification, Sedimentology 55 (1) (2008) 31–63.

[41] C.Y. Kuo, J.D. Frost, J.S. Lai, L.B. Wang, Three-Dimensional Image Analysis of Aggregate Particles from Orthogonal Projections, Transp. Res. Rec. 1526 (1) (1996) 98–103.

[42] G.H. Bagheri, C. Bonadonna, I. Manzella, P. Vonlanthen, On the characterization of size and shape of irregular particles, Powder Technol. 270 (2015) 141–153.

[43] J. Adam, E. Antonakou, A. Lappas, M. Stöcker, M.H. Nilsen, A. Bouzga, et al., In situ catalytic upgrading of biomass derived fast pyrolysis vapours in a fixed bed reactor using mesoporous materials, Microporous Mesoporous Mater. 96 (1) (2006) 93–101.

[44] A. Karim, J. Bravo, D. Gorm, T. Conant, A. Datye, Comparison of wall-coated and packed-bed reactors for steam reforming of methanol, Catal. Today 110 (1) (2005) 86–91.

[45] J.A. Botas, J.A. Melero, F. Martínez, M.I. Pariente, Assessment of Fe2O3/SiO2 catalysts for the continuous treatment of phenol aqueous solutions in a fixed bed reactor, Catal. Today 149 (3) (2010) 334–340.

[46] P. Cnudde, R. Demuynck, S. Vandenbrande, M. Waroquier, G. Sastre, V.V. Speybroeck, Light Olefin Diffusion during the MTO Process on H-SAPO-34: A Complex Interplay of Molecular Factors, J. Am. Chem. Soc. 142 (13) (2020) 6007–6017.

[47] Z. Liu, H. Li, T. Zhang, Y. Wang, P. Shi, Y. Wang, et al., Mother liquor induced preparation of SAPO-34 zeolite for MTO reaction, Catal. Today 358 (2020) 109–115.

[48] M.E. Potter, L.-M. Armstrong, R. Raja, Combining catalysis and computational fluid dynamics towards improved process design for ethanol dehydration, Cat. Sci. Technol. 8 (23) (2018) 6163–6172.

[49] E.N. Landis, D.T. Keane, X-ray microtomography, Mater. Charact. 61 (12) (2010) 1305–1316.

[50] C.A. Schneider, W.S. Rasband, K.W. Eliceiri, NIH Image to ImageJ: 25 years of image analysis, Nat. Methods 9 (7) (2012) 671–675.

[51] W.R. Tiago Ferreira, ImageJ User Guide. ImageJ User Guide IJ 146r, 2012.

[52] ThermoFisher Scientific. Avizo Software User's Guide. Avizo Software User's Guide, 2019.

[53] D.J. Patil, J. Smit, A.M. van Sint, J.A.M. Kuipers, Wall-to-bed heat transfer in gas–solid bubbling fluidized beds, AIChE J 52 (1) (2006) 58–74.

[54] M.E. Potter, L.-M. Armstrong, M. Carravetta, T.M. Mezza, R. Raja, Designing Multi-Dopant Species in Microporous Architectures to Probe Reaction Pathways in Solid-Acid Catalysis, Front. Chem. 8 (171) (2020).

[55] M.E. Potter, M.E. Cholerton, J. Kezina, R. Bounds, M. Carravetta, M. Manzoli et al., Role of Isolated Acid Sites and Influence of Pore Diameter in the Low-Temperature Dehydration of Ethanol. 4(11) (2014) 4161-4169.

[56] E. Achenbach, Heat and flow characteristics of packed beds, Exp. Therm. Fluid Sci. 10 (1) (1995) 17–27.

[57] A.G. Dixon, Correlations for wall and particle shape effects on fixed bed bulk voidage, Can. J. Chem. Eng. 66 (5) (1988) 705–708.

[58] S. Kyrimis, M.E. Potter, R. Raja, L.-M. Armstrong, Understanding catalytic CO2 and CO conversion into methanol using computational fluid dynamics, Faraday Discuss. (2021).